High-Gain Low-Noise Phototransistors Based on Solution-Processed Bi$_2$S$_3$ Nanocrystals

Yujie Yang[1,2] Zhenglin Jia[1,2] Yanyan Li[1,2] Ruiming Li,[1,2] Yong Liu[1,2] Fang Yao,[1,2]
Xiangming Fang,[3] Huiming Huang,[1] and Qianqian Lin[1,2,*]

[1]*Key Lab of Artificial Micro- and Nano-Structures of Ministry of Education of China, School of Physics and Technology, Wuhan University, Wuhan 430072, P. R. China*
[2]*Hubei Luojia Laboratory, Wuhan 430072, P. R. China*
[3]*Department of Materials and Chemical Engineering, Taiyuan University, Taiyuan 030032, P. R. China*

Chalcogenide-based semiconductors have recently emerged as promising optoelectronic materials. In particular, bismuth-based sulfides have demonstrated great potential for device applications, such as in photovoltaics and photodetection. However, most of the devices reported have been based on silver-bismuth-sulfide-based solar cells. Work on bismuth sulfide based on precursor methods has been barely reported, and studies of its optoelectronic properties are lagging far behind. In this paper, we first report solution processing of Bi$_2$S$_3$ thin films, describe the systematic optimization of the precursors, and investigate the influence of composition and annealing on the properties of the films, including their morphology, crystallinity, charge-carrier dynamics, charge transport, and photoconductive gain. We also demonstrate excellent field-effect transistors based on Bi$_2$S$_3$ thin films, and introduce the use of these Bi$_2$S$_3$ phototransistors for weak-light detection. The optimized devices exhibit extremely high responsivity and low dark current, paving the way for high-performance photodetection.

I. INTRODUCTION

Chalcolgenide-based optoelectronic materials, e.g., binary CdTe [1,2], Sb$_2$S$_3$ [3–5], Bi$_2$S$_3$ [6,7], ternary CuSbS$_2$ [8], AgSbS$_2$ [9,10], NaBiS$_2$ [11], and AgBiS$_2$ [12,13], have recently demonstrated great potential for optoelectronic applications, benefiting mainly from their low cost, superior stability, tunable optoelectronic properties, and facile processability. Antimony- and bismuth-based chalcogenide thin films have exhibited fairly good device performance on multiple platforms, including photovoltaics [6,14,15], photodetectors [5,16,17], field-effect transistors (FETs) [4,5] and photocalalysts [18,19]. Furthermore, these chalcogenide thin films can be easily processed by various approaches, such as thermal evaporation [20], chemical-bath deposition [21], hydrothermal processing [22–24], spin-coating of quantum dots [25], and the use of precursors [26–28]. Among these methods, vacuum-based techniques have higher equipment and processing costs. Chemical-bath deposition and hydrothermal methods require large amount of solutions and complicated fabrication procedures. Spin-coating is a facile approach, and has excellent repeatability in tuning the composition and film thickness. In particular, solar cells based on silver bismuth sulfide (AgBiS$_2$) have achieved compelling device performance, and the power conversion efficiency has reached more than 9% (certified) [12]. However, such high efficiency was achieved based on the quantum dot strategy, which requires sophisticated synthesis and is still suffering from instability of the quantum dot solution, and the charge transport can be highly affected by ligands.

Devices based on precursors possess relatively poor device performance. In addition, the reported chalcogenide-based phototransistors have either been fabricated based on other FET channels [10] or been mixed with additional transport materials [29]. Most of the chalcogenides do not exhibit proper transfer curves when they are deposited as channel layers. Only a few papers have reported field-effect transistors based on Bi$_2$S$_3$ [30,31] and Bi$_2$Se$_3$ [32] single-crystalline nanowires. Furthermore, the solution processing of Bi$_2$S$_3$ thin films is still challenging, due to the highly anisotropic crystallinity and the stoichiometric imbalance induced by sulfur or bismuth vacancies (i.e., defects). It has been reported that highly crystalline Bi$_2$Se$_3$ nanoribbons can be prepared via a solvothermal method [33]. However, nanostructured Bi$_2$Se$_3$ samples are not favorable for device fabrication. More importantly, the understanding of the fundamental properties of Bi$_2$S$_3$ is still limited, and new insights into charge-carrier dynamics and charge transport

---

*q.lin@whu.edu.cn

are urgently needed to further improve the performance of devices based on it.

To address these issues, we introduce a sol-gel method to form Bi_2S_3 nanocrystals, and systematically investigate the composition of the precursors and the annealing conditions to carefully tune the morphology, crystallinity, and optoelectronic properties. Then, we study the charge-transport properties using time-resolved microwave conductivity (TRMC) [34] and temperature-dependent photoconductivity. We also fabricate field-effect transistors based on the spin-coating of ultrathin Bi_2S_3 layers used as the charge-transport channel, and investigate the influence of the thiourea-bismuth (S-Bi) ratio and thermal annealing on the device performance of Bi_2S_3-based FETs. Furthermore, we introduce the use of these Bi_2S_3 transistors for photodetection, and try to further improve the responsivity and reduce the dark current and noise.

II. EXPERIMENTAL PROCEDURES

A. Materials

Bismuth nitrate pentahydrate $[Bi(NO_3)_3 \cdot 5H_2O, 98.0\%]$ is purchased from Sigma Aldrich. Thiourea $(CH_4N_2S, 99\%)$ is purchased from Sinopharm. 2-Methoxyethanol ether (99%) is purchased from Aladdin. The Si substrate $[SiO_2(300 \text{ nm})/Si(725 \text{ } \mu m)]$ is purchased from Kaihua Silicon Wafer Corp.

B. Device fabrication

All devices are fabricated based on precleaned SiO_2/Si substrates, and thin-film transistors (TFTs) are fabricated based on a bottom-gate-top-contact configuration. The substrates are cleaned with deionized water and ethanol with successive sonication, and dried with dry air. Then the substrates are treated with UV radiation and ozone for 15 min. To deposit the channel layers, 0.2 mmol of $Bi(NO_3)_3 \cdot 5H_2O$ is dissolved in 1 ml of 2-methoxyethanol. Then 0.3 mmol of thiourea (TU) (CH_4N_2S) is added to the solution. By adding different amounts of CH_4N_2S, we can obtain precursors with different Bi-S ratios. Subsequently, Bi_2S_3 solutions with different S contents are spin-coated via spin-coating at 5000 rpm for 40 s on commercial Si substrates. The films obtained are annealed at $100\,^{\circ}C$ for 10 min in a glove box and further annealed at $280\,^{\circ}C$ for 10 min in air. Finally, 25 nm of C_{60} and 60 nm of Al are thermally deposited through shadow masks as electrodes. The channel length (L) and width (W) of the TFTs are 100 μm and 2 mm, respectively.

C. Material characterization

The transmittance and reflectance are acquired based on measured transmittance and reflectance spectra (Lambda 1050 spectrometer, Perkin Elmer). The surface morphology of the Bi_2S_3 films is studied with a field-emission

scanning electron microscope (Zeiss GeminiSEM 500). The crystal phases of the Bi_2S_3 for various TU contents are indexed by use of x-ray diffraction (XRD, D8 Advance x-ray diffractometer). The thickness and roughness of the Bi_2S_3 films obtained are measured with a profilometer (Alpha-Step D-500). The photoconductivity of the Bi_2S_3 films is tested with a semiconductor analyzer (Keysight, B1500A) under white LED illumination (Thorlabs). The temperature is modulated with a cryostat (Instec, LN2-P4C, C100W) under vacuum.

D. Device characterization

The electrical performance of the TFTs, such as the transfer curves, output curves, noise current, external quantum efficiency (EQE), and response times, is collected with a semiconductor analyzer (Keysight, B1500A) at $-20\,^{\circ}C$. The temperature-dependent transfer curves are measured with a semiconductor analyzer (Keysight, B1500A), and the temperature is controlled with a cryostat (Instec, mK2000B, LN2-P4C,C100W) under vacuum. The optoelectronic performance of the devices, including light-intensity-dependent transfer curves and output curves, is tested via a semiconductor analyzer (Keysight, B1500A) under LED illumination (Thorlabs).

III. RESULTS AND DISCUSSION

In the work presented here, we develop a new precursor route to depositing uniform high-quality Bi_2S_3 thin films. The Bi_2S_3 precursors are prepared by dissolving bismuth nitrate $[Bi(NO_3)_3 \cdot 5H_2O]$ in 2-methoxyethanol. Then, various amounts of TU are added to the bismuth nitrate solution to form a Bi_2S_3 sol [35] (see Supplementary Note 1 [36] for more details); we can clearly observe the transparent solution change to yellow, indicating the formation of Bi_2S_3 nanocrystal seeds (see Supplementary Video 1 [36]). It is also worth noting that with an increase in the thiourea-bismuth (S-Bi) ratio, the color of the Bi_2S_3 precursor changes from light yellow to brown, as shown in Fig. S1(a). We then spin-coat the prepared precursor and thermally anneal the precursor film using a two-step approach; that is, we preanneal the film at a low temperature (around $100\,^{\circ}C$) for a short time (10 min) and then fully anneal the preannealed film at an elevated temperature (greater than $200\,^{\circ}C$) for a certain time (3–15 min). Figure 1(a) depicts these processes schematically, and Fig. S1(b) displays optical images of Bi_2S_3 deposited with precursors containing various S-Bi ratios.

Interestingly, the color of the Bi_2S_3 thin films obtained also becomes darker with an increase in the amount of TU in the precursor. Figure S2 shows the surface roughness of these films recorded with a profilometer, and all of these films show similar values of approximately 3 nm. However, the films prepared with an S-Bi ratio of 1.5 exhibit a relatively small variation, and the films prepared with a
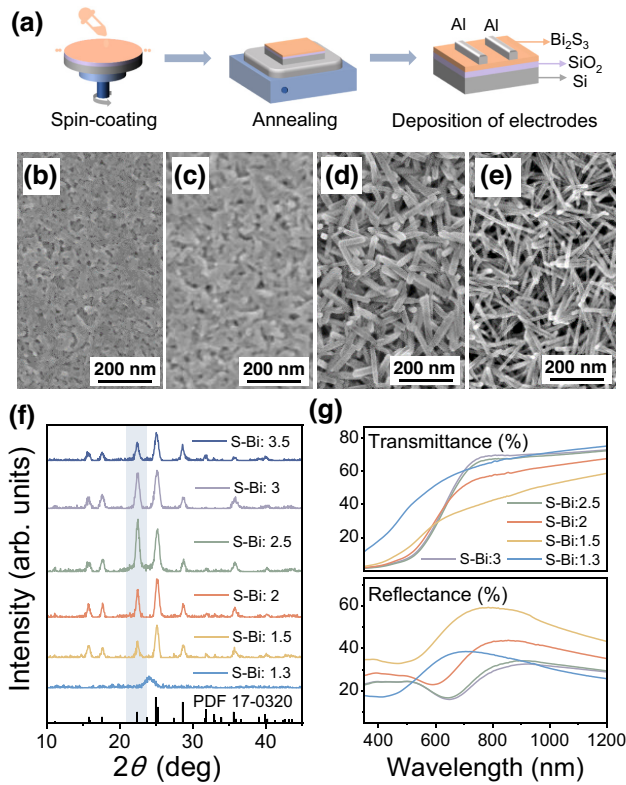
FIG. 1. (a) Schematic illustration of the processing of Bi_2S_3 thin films and FET devices. (b)–(e) Comparison of scanning-electron-microscope images of Bi_2S_3 thin films prepared with various S-Bi ratios: (b) 1.5, (c) 1.8, (d) 2, (e) 3. (f) Recorded XRD patterns. (g) Transmittance and reflectance spectra of these thin films with gradually increasing S-Bi ratio.

large S-Bi ratio (2.5 or 3) show a large fluctuation. Figure S3 displays spin-coated large-area Bi_2S_3 films on flexible substrates, indicating fairly good uniformity and superior processability on various substrates.

To further identify the morphology differences, we perform scanning-electron-microscopy (SEM) measurements, as shown in Figs. 1(b)–1(d). Intriguingly, we find that the films obtained possess increased numbers of pinholes with an increased S-Bi ratio. The Bi_2S_3 films spin-coated with large S-Bi ratios show a typical nanorod structure, and the films become porous. In addition, the diameter decreases but the length of the nanorods increases when the S-Bi ratio is increased from 1.8 to 3. In contrast, the Bi_2S_3 films prepared with an S-Bi ratio of 1.5 are dense with minimal pinholes, despite the small grain size. In addition, we also compare the crystallinity by recording x-ray diffraction patterns, as shown in Fig. 1(f). All of these films exhibit a typical Bi_2S_3 crystal structure, and the characteristic peaks match well with the standard Joint Committee on Powder Diffraction Standards card for the Bi_2S_3 XRD pattern (PDF 17-0320). We also find that the XRD intensity increases gradually when the S-Bi ratio is increased

from 1.3 to 2.5. However, the XRD intensity decreases slightly when the S-Bi ratio is increased further from 2.5 to 3, which is consistent with the SEM results. In addition, we also determine the crystallinity of these films based on the ratio between the area of the crystalline peaks (A_c) and the sum of the areas of the amorphous (A_a) and crystalline peaks, according to

$$\chi_c = \frac{A_c}{A_c + A_a}. \tag{1}$$

Interestingly, we also find a decreased crystallinity when the S-Bi ratio is larger than 2.5, as shown in Fig. S4. Furthermore, Fig. 1(g) presents transmittance and reflectance spectra of Bi_2S_3 films prepared with various S-Bi ratios. The absorption edge is redshifted for the high-S-Bi-ratio films, which is in line with the recorded optical images. More importantly, the samples prepared with an S-Bi ratio of 1.5 exhibit the largest reflectance, reflecting a high refractive index (corresponding to, e.g., high crystallinity and high density) and low scattering losses.

As aforementioned, understanding the charge-carrier dynamics and charge-transport properties is critical to elucidating the working mechanism and providing key messages for designing optoelectronic devices. Here, we introduce the use of TRMC to evaluate the fundamental properties of the charge carriers, as shown in Fig. 2. TRMC measurement is a contactless technique and can probe the charge-carrier dynamics of various semiconductors [37–39]. The thin-film 7samples are excited with a fast laser pulse (approximately 5 ns), which generates a certain amount of carriers within the semiconductor thin film and leads to absorption of microwaves. Then, the transmittance or reflectance of the microwaves can be monitored as a function of time after photoexcitation, resulting in measurement of the decay. To enhance the microwave sensitivity, we introduce a high-Q microwave cavity, which has a resonance frequency of approximately 4.3 GHz. Note that the resonance frequency is mainly determined by the microwave cavity, and is tuned with a tuning screw. We also measure the TRMC decay at approximately 8.6 GHz (as shown in Fig. S5), which is consistent with the results obtained from the measurements at approximately 4.3 GHz. The source power of the microwaves is set to 1 mW, and the excitation laser wavelength is 532 nm, with a tunable pulse fluence of 0.01–100 $\mu J\,cm^{-2}$. The changes in the microwave conductivity of the samples can be correlated with the changes in the detected microwave power by use of a sensitivity factor K [38] (see Supplementary Note 2 [36] for more details) as follows:

$$\frac{\Delta P(t)}{P} = -K\,\Delta G(t), \tag{2}$$

where $\Delta P(t)/P$ is the change in the detected microwave power and $\Delta G(t)$ is the change in the conductance. Based
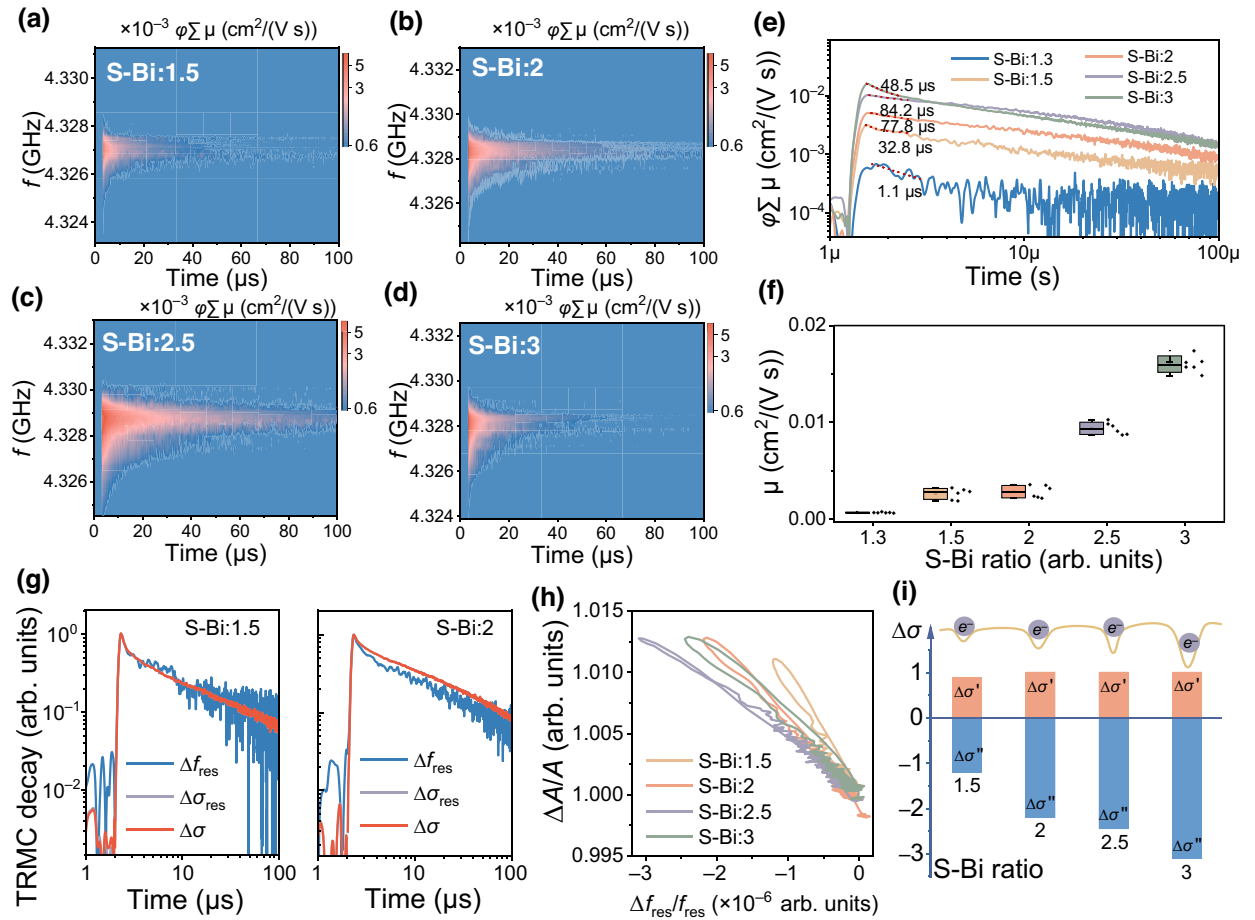
FIG. 2.   (a)–(d) Comparison of two-dimensional (2D) TRMC spectra of Bi_2S_3 thin films prepared with various S-Bi ratios (at a fluence of approximately 5 $\mu J/cm^2$): (a) 1.5, (b) 2, (c) 2.5, (d) 3. Comparison of (e) TRMC decay (at a fluence of approximately 5 $\mu J/cm^2$) at the resonance frequency and (f) $\varphi \sum \mu$ for Bi_2S_3 thin films prepared with gradually increasing S-Bi ratios (1.3–3). (g) Comparison of the hysteresis loops of the complex photoconductivity of Bi_2S_3 thin films prepared with varying S-Bi ratios. (h) Real and imaginary parts of the photoconductive decay of samples based on S-Bi ratios of 1.5 and 2. (i) Schematic illustration of the energetic depth of the trap states.

on the maximum change in the conductance and the incident light intensity (I_0), we can determine the mixed mobility ($\sum \mu$) as follows [40]:

$$\varphi \sum \mu = \frac{\Delta G_{\mathrm{max}}}{I_0 \beta_{\mathrm{TRMC}} e F_A}, \tag{3}$$

where φ is the charge-carrier generation yield, β_{TRMC} is the ratio between the broad and narrow inner dimensions of the waveguide, e is the elementary charge, and F_A is the optical attenuation.

Specifically, we record the 2D TRMC spectra of Bi_2S_3 thin films prepared with various S-Bi ratios, as shown in Figs. 2(a)–2(d), and Fig. 2(g) shows typical time-resolved TRMC decays extracted at the resonance frequency (f_{res}). Similarly to the trend observed by SEM and XRD, the TRMC lifetime increases first until the S-Bi ratio reaches 2.5, and then decreases slightly when the S-Bi ratio is 3. In contrast, the TRMC amplitude (proportional to the

mobility) increases gradually up to an S-Bi ratio of 3, as shown in Figs. 2(e) and 2(f). We also fit the fitted initial TRMC decays, shown in Fig. 2(e), and extract the photoconductivity charge-carrier lifetimes by using a single exponential function. The increased product of the generation yield and mobility ($\varphi \sum \mu$) and the increased lifetime are attributed mainly to the enhanced crystallinity and increased grain size. The reduced charge-carrier lifetime of the Bi_2S_3 samples prepared with a large S-Bi ratio can be attributed to the increased number of grain boundaries and increased surface area. To further reveal the complex photoconductivity of the solution-processed Bi_2S_3 thin films, we also decouple the photoconductive effect and photodielectric effect by resolving the frequency shift (Δf_0) and the amplitude change (ΔA) as a function of time. These values are normalized to the initial resonance frequency (f_0) and amplitude (A). Then, we plot the hysteresis loop and also compare the real and imaginary parts of the photoconductivity, as shown in Fig. 2(h). The

complex photoconductivity is a sign of the energetic depth of the traps [41,42]. Interestingly, we find that the imaginary part of the photoconductivity increases gradually with increased S-Bi ratio. However, the real part of the photoconductivity does not change much. The TRMC decay also implies that the samples with an excessive amount of TU show a faster imaginary photoconductive decay. Based on these observations, we can qualitatively compare the shallow and deep traps based on the relative values of the normalized amplitude change and frequency shift for these Bi_2S_3 thin films, as shown in Fig. 2(i). This suggests that the Bi_2S_3 thin films prepared with large S-Bi ratios may have an increased amount of relatively deeper trap states, assuming that the crystal grain size and shape do not affect the charge transport [43]. However, it is also worth noting that the morphology of the crystal grains may also influence the imaginary part of the photoconductivity to some extent. Additionally, we study the influence of the annealing time (in the second stage, at 280 °C) on the charge-carrier dynamics, as shown in Fig. S6. The charge-carrier lifetime increases with an increase in the annealing time, which could also be related to the improved crystallinity. Moreover, the recorded photoconductive gain of Bi_2S_3 photoconductors annealed for 10 min showed a higher *on:off* ratio and a reduced dark conductivity (Fig. S7), suggesting full conversion of the amorphous state. Based on the above analysis of the TRMC, we can retrieve basic information about both $\varphi \sum \mu$ and the lifetime (τ) within the Bi_2S_3 crystal grains; these are the quantities that mainly determine the photoconductive gain in operational devices, given by

$$\text{gain} = \frac{\tau}{t_{tr}} = \frac{\mu \tau V}{L^2}, \qquad (4)$$

where τ is the carrier lifetime, t_{tr} is the carrier transit time, μ is the carrier mobility, L is the channel length, and V is the bias voltage. Ideally, a large mobility and long lifetime are desirable for high-performance photodetection. However, the real charge transport within a device is also significantly affected by the morphology. The porous nature of Bi_2S_3 films composed of nanoribbons significantly reduces the charge-transport channel in an FET. Hence, there is a trade-off between charge-carrier dynamics and morphology in real cases.

Having knowledge of the optoelectronic properties, we now turn to the consideration of devices. A set of thin-film transistors are fabricated based on silicon substrates with thin SiO_2 layers on top. Note that a thin layer of C_{60} (25 nm) is deposited to isolate the Al electrodes from direct contact with the Bi_2S_3 layer, as the hot Al vapor may react during evaporation with the excess S in the Bi_2S_3 thin film. We also measure the typical transfer curves of FETs fabricated without a C_{60} interlayer, as shown in Fig. S8. These devices show a much higher *off*-state current, indicating
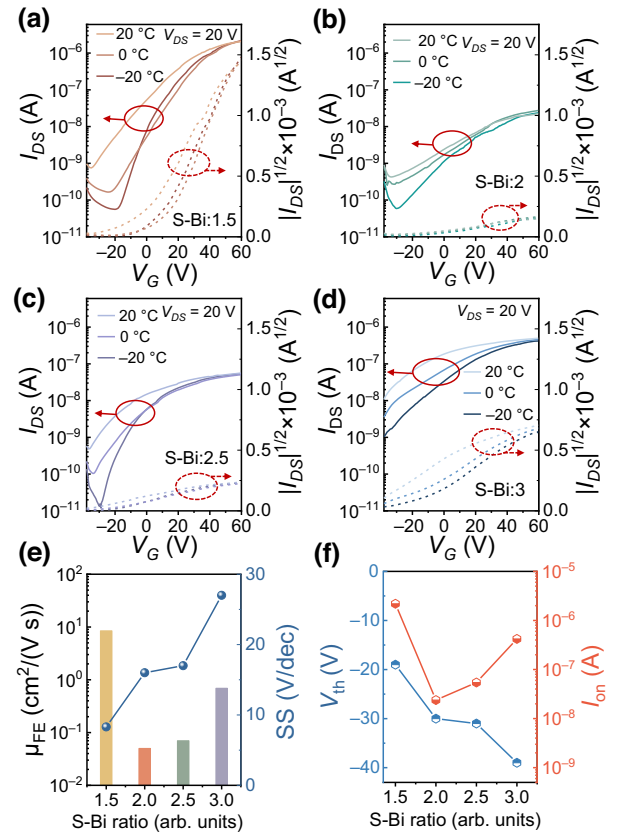

FIG. 3. (a)–(d) Temperature-dependent transfer curves of FETs fabricated based on Bi_2S_3 thin films with various S-Bi ratios: (a) 1.5, (b) 2, (c) 2.5, and (d) 3. (e) FET mobility and subthreshold swing. (f) V_{th} and I_{on} of Bi_2S_3 FETs fabricated with various S-Bi ratios.

that the FETs cannot be fully switched off. We first compare the impact of the S-Bi ratio on the device performance (Fig. 3), and find that the transfer curves deteriorate with an increase in the TU content of the precursor, and we do not observe any transfer curves for devices based on an S-Bi ratio of 1.3. In addition, the *off*-state current of these high-S-Bi-ratio FETs cannot be fully switched off, and the turned-on current is reduced, due mainly to the porous nature of the channels. We also compare the inferred FET mobility [44], subthreshold swing (SS), turn-on voltage (V_{th}), and turned-on current (I_{on}) for devices prepared with various S-Bi ratios, as shown in Figs. 3(e) and 3(f). It is found the devices based on an S-Bi ratio of 1.5 exhibit the smallest SS and the highest FET mobility and I_{on}. The turn-on voltage shifts to larger reverse bias voltage with an increase in the S-Bi ratio. Not surprisingly, the devices based on Bi_2S_3 prepared with an S-Bi ratio of 1.5 show fairly good transfer curves, benefiting mainly from the dense morphology, relatively high crystallinity, fairly good charge transport, and shallow nature of the traps. In addition, we compare the S-Bi-ratio-dependent device performance, e.g., the responsivity (R) and the specific
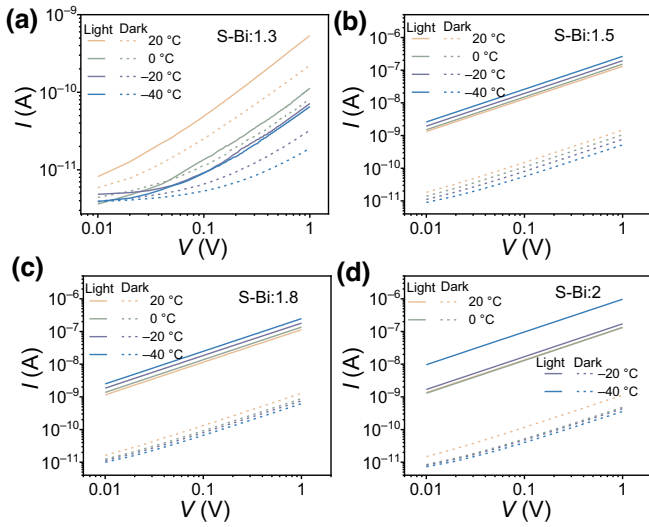
FIG. 4. Temperature-dependent dark conductivity and photoconductivity under white LED illumination of Bi_2S_3 thin films prepared with various S-Bi ratios: (a) 1.3, (b) 1.5, (c) 1.8, (d) 2.

FIG. 5. Fitting of the temperature-dependent dark conductivity and photoconductivity of Bi_2S_3 thin films prepared with various S-Bi ratios: (a) 1.3, (b) 1.5, (c) 1.8, (d) 2.

detectivity (D^*), given by

$$D^* = \frac{R\sqrt{A}}{i_{\text{noise}}}, \qquad (5)$$

where A is the device area. It is found that the responsivity decreases slightly when the S-Bi ratio is increased to 2, and increases slightly with a further increase in the S-Bi ratio (Fig. S9). However, the noise density increases significantly with an increase in the S-Bi ratio. The observed trend can be attributed to the changes in mobility, carrier lifetime, and also morphology, which suggests that the device with an S-Bi ratio of 1.5 shows the highest specific detectivity. Moreover, all of these devices show a slight temperature dependence, but this is not so prominent as in the case of single-crystal devices [31]. To further elucidate the underlying mechanism, we perform measurements of the conductivity of these Bi_2S_3 thin films, as shown in Fig. S10.

Compared with the dark current, the devices based on Bi_2S_3 with an S-Bi ratio of 1.3 do not show noticeable photoconductivity, mainly due to insufficient crystallization and the deficit of S. The photoconductors based on Bi_2S_3 with an S-Bi ratio of 1.5 exhibit the largest *on:off* ratio, and with a further increase in the S-Bi ratio, the photocurrent does not show a significant increase, but the dark current increases with an increase in the TU content of the precursor, suggesting that the S source is excessive and results in S-rich phases. We also conduct temperature-dependent photoconductive measurements, as shown in Fig. 4, which confirm a similar trend in the dependence on the S-Bi ratio, and the calculated activation energy in the dark for these Bi_2S_3 photoconductors also decreases with an increase in the S-Bi ratio, as shown in Fig. 5. The

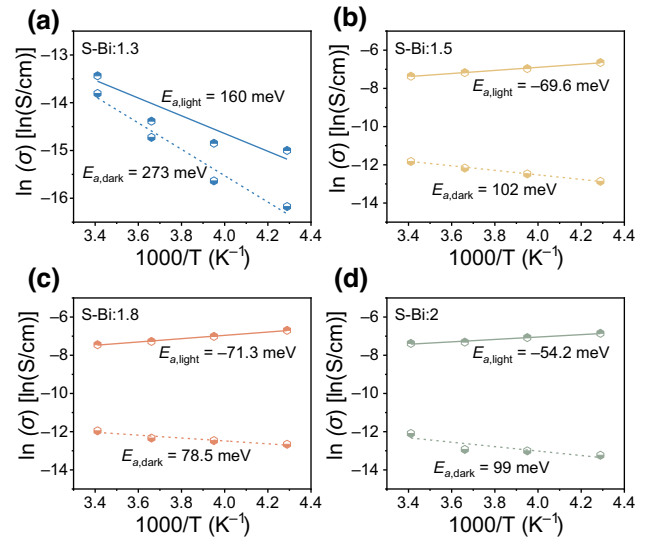positive activation energy is mainly due to the reduced thermalized carrier density at low temperature. More interestingly, the activation energy of the photoconductivity changes to negative when the S-Bi ratio is greater than 1.5, indicating that the charge-transport mode can be switched from a localized-state-induced "hopping" mechanism to a more "bandlike" transport [45,46]. The photoconductivity is independent of the carrier density, as the number of dark carriers (n_{dark}) is much less than the photoexcited carrier density (n_{ph}), which is the same for all samples at various temperatures. Hence, the change in the conductivity σ should be attributed mainly to a change in the mobility μ, given by

$$\sigma_{\text{ph}} = (n_{\text{dark}} + n_{\text{ph}})q\mu \approx n_{\text{ph}}q\mu. \qquad (6)$$

The S vacancies caused by a S deficit could introduce a large number of deep-level trap states [47] and result in "hopping" transport [48,49]. According to the literature on chalcogenides, localized defects can be effectively eliminated by sulfurization [50]. Hence, an S-Bi ratio greater than 1.5 is required to facilitate charge transport. Furthermore, the sample with a S-Bi ratio of 2, with excess S, also shows a slightly increased activation energy, indicating deteriorated charge transport at a high S-Bi ratio, which is also consistent with the FET performance.

Considering that excellent charge transport, the highest photoconductive gain, and the best FET performance are obtained with Bi_2S_3 with a stoichiometric S-Bi ratio of 1.5, we systematically characterize the performance metrics of phototransistors fabricated with this precursor composition at a thermoelectric-cooling temperature of $-20\,^{\circ}\text{C}$. Figure 6(a) displays a contour plot of the photosensitivity
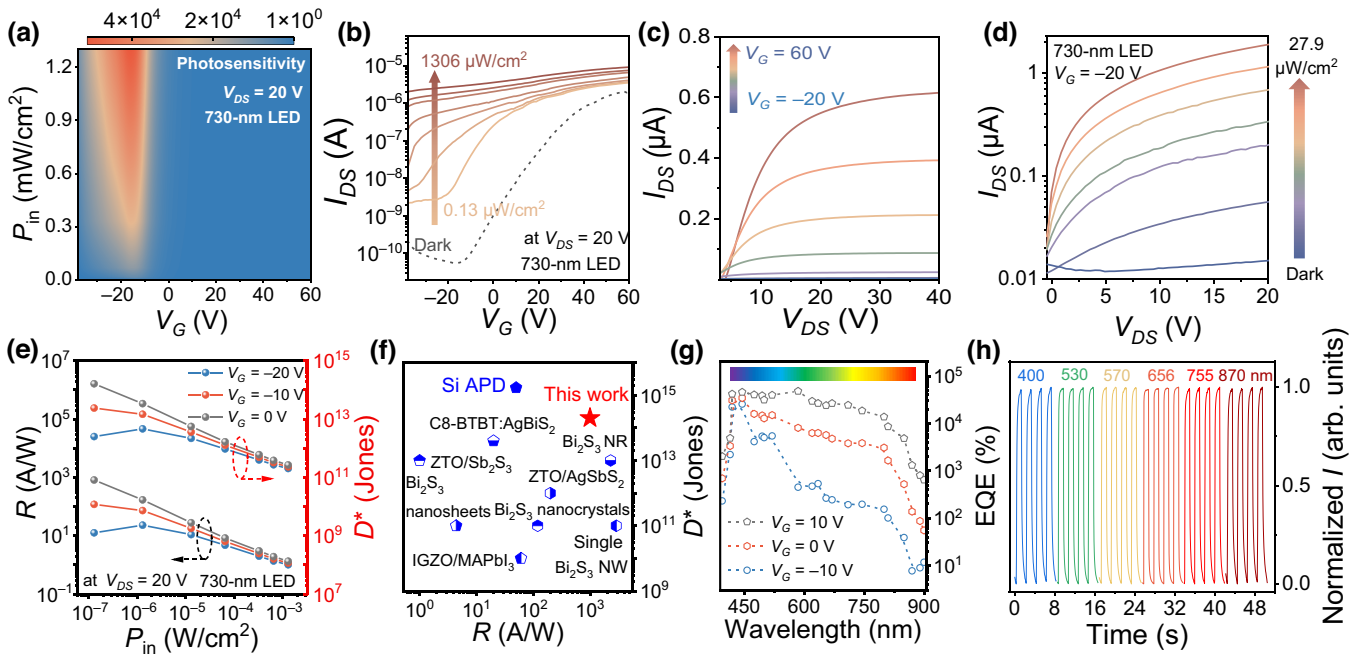
FIG. 6. (a) Contour plot of photosensitivity, (b) light-intensity-dependent transfer curves, (c) gate-voltage-dependent output curves, (d) light-intensity-dependent output curves, (e) light-intensity-dependent responsivity and specific detectivity, (f) comparison of the specific detectivity [Avalanche Photodiode (APD), 2,7-dioctyl benzothieno [3,2- b]benzothiophene (C8-BTBT), Nanorods (NR), Zinc-Tin Oxide (ZTO), Indium Gallium Zinc Oxide (IGZO), Nanowire (NW)], (g) EQE spectra, and (h) temporal photoresponses under illumination at various wavelengths of optimized Bi_2S_3 phototransistors fabricated based on an S-Bi ratio of 1.5.

as a function of the incident light intensity (P_{in}) and gate voltage (V_G) under illumination with a 730-nm LED.

Figures 6(b)–6(d) present the light-intensity-dependent transfer curves and gate-voltage-modulated and light-intensity-dependent output curves, which suggest that the optimized Bi_2S_3 FETs can be very sensitive to incident photons and that the devices can also be well tuned by the gate voltage. Similarly, we also present the transfer curves and photosensitivity under blue (400 nm) and green (530 nm) light in Fig. S11. Figure 6(e) presents the light-intensity-dependent responsivity, which shows the typical P_{in}-dependent responsivity of phototransistors, that is, the responsivity decreases with an increase in light intensity. This nonlinearity has been well recognized in the field of photoconductors and phototransistors, and can be attributed to increased recombination losses at high irradiance [51]. The highest responsivity can reach 1000 A/W under extremely weak illumination. We also record the noise spectra of the optimized devices, as shown in Fig. S12, based on which we can further determine the specific detectivity. The calculated detectivity is shown in Fig. 6(e), and the highest D^* reaches 10^{14} Jones, which is the highest value found, compared with literature reports [Fig. 6(f)] [4,10,29,52–56]. Figure 6(g) displays the EQE spectra of the Bi_2S_3 phototransistors, and temporal photoresponses of the devices under illumination at various wavelengths are shown in Fig. 6(h); these

results show a relatively high EQE and fast photoresponse covering the whole visible and near-infrared regions. Figure S13 displays the transient photocurrent of the FETs under illumination with a 100-Hz-modulated 650-nm LED. The rise times (t_r) and fall times (t_f) of the devices are determined to be 152 and 270 µs, respectively. The response time is relatively slow compared with that of photodiodes. However, the response time could be enhanced by reducing the transport-channel width and increasing the bias voltage. Considering the extremely high responsivity and detectivity, we also evaluate the capability of these phototransistors for weak-light detection. The transfer curves of the Bi_2S_3 phototransistors show a clear increase even under weak illumination of 500 pW/cm^2, as shown in Fig. S14, indicating ultrahigh photosensitivity and great potential for weak-light detection, in fields such as security monitoring, light communication, and medical diagnosis.

IV. CONCLUSION

In conclusion, we develop a facile solution-processing technique for depositing high-quality Bi_2S_3 thin films, and the nanocrystal morphology, crystallinity, and optoelectronic properties can be easily tuned by optimizing the S-Bi ratio in the precursors and the thermal-annealing conditions. Achieving the stoichiometric S-Bi ratio is found to be critical to addressing the stoichiometric-imbalance

issue and has a profound impact on high-performance Bi_2S_3-based photoconductors and field-effect transistors, since both S-rich and Bi-rich compositions can be detrimental and can easily result in the formation of trap states. We also systematically investigate the charge-carrier dynamics of the Bi_2S_3 thin films, and features of the carrier lifetime, mobility, and traps are revealed. Furthermore, we fabricate ultrasensitive phototransistors based on optimized Bi_2S_3 thin films, and achieve a high detectivity, which shows great potential for weak-light detection.

ACKNOWLEDGMENTS

[1] J. M. Burst, J. N. Duenow, D. S. Albin, E. Colegrove, M. O. Reese, J. A. Aguiar, C. S. Jiang, M. K. Patel, M. M. Al-Jassim, D. Kuciauskas, S. Swain, T. Ablekim, K. G. Lynn, and W. K. Metzger, CdTe solar cells with open-circuit voltage breaking the 1 V barrier, Nat. Energy **1,** 16015 (2016).

[2] L. Shen, Y. Fang, H. Wei, Y. Yuan, and J. Huang, A highly sensitive narrowband nanocomposite photodetector with gain, Adv. Mater. **28,** 2043 (2016).

[3] R. Kondrotas, C. Chen, and J. Tang, Sb_2S_3 solar cells, Joule **2,** 857 (2018).

[4] H. Huang, Y. Yang, H. Chen, F. Qin, B. Yu, R. Wang, Q. Cao, T. Wang, and Q. Lin, Interfacial engineering of high-performance, solution-processed Sb_2S_3 phototransistors, ACS Appl. Mater. Interfaces **14,** 57419 (2022).

[5] K. Zhao, J. Yang, M. Zhong, Q. Gao, Y. Wang, X. Wang, W. Shen, C. Hu, K. Wang, G. Shen, M. Li, J. Wang, W. Hu, and Z. Wei, Direct polarimetric image sensor and wide spectral response based on quasi-1D Sb_2S_3 nanowire, Adv. Funct. Mater. **31,** 2006601 (2020).

[6] H. Moreno-Garcia, M. T. S. Nair, and P. K. Nair, All-chemically deposited Bi_2S_3/PbS solar cells, Thin Solid Films **519,** 7364 (2011).

[7] W. Yang, J. Yang, K. Zhao, Q. Gao, L. Liu, Z. Zhou, S. Hou, X. Wang, G. Shen, X. Pang, Q. Xu, and Z. Wei, Low-noise dual-band polarimetric image sensor based on 1D Bi_2S_3 nanowire, Adv. Sci. **8,** e2100075 (2021).

[8] Y. Xu, Q. Ye, W. Chen, X. Pan, L. Hu, S. Yang, T. Hayat, A. Alsaedi, J. Zhu, and S. Dai, Solution-processed $CuSbS_2$ solar cells based on metal-organic molecular solution precursors, J. Mater. Sci. **53,** 2016 (2017).

[9] L. Zhang, C. Zhu, and T. Chen, Solution processed $AgSbS_2$ film for efficient planar heterojunction solar cells, Appl. Phys. Lett. **119,** 151906 (2021).

[10] Y. Yang, H. Huang, S. Bai, F. Yao, and Q. Lin, Opto-electronic modulation of silver antimony sulfide thin films for photodetection, J. Phys. Chem. Lett. **13,** 8086 (2022).

[11] Y. T. Huang, *et al.*, Strong absorption and ultrafast localisation in $NaBiS_2$ nanocrystals with slow charge-carrier recombination, Nat. Commun. **13,** 4960 (2022).

[12] Y. Wang, S. R. Kavanagh, I. Burgues-Ceballos, A. Walsh, D. O. Scanlon, and G. Konstantatos, Cation disorder engineering yields $AgBiS_2$ nanocrystals with enhanced optical absorption for efficient ultrathin solar cells, Nat. Photonics **16,** 235 (2022).

[13] S. Akhil and R. G. Balakrishna, $AgBiS_2$ as a photoabsorber for eco-friendly solar cells: A review, J. Mater. Chem. A **10,** 8615 (2022).

[14] Y. Qi, Y. Li, and Q. Lin, Engineering the charge extraction and trap states of Sb_2S_3 solar cells, Appl. Phys. Lett. **120,** 221102 (2022).

[15] R. Tang, X. Wang, W. Lian, J. Huang, Q. Wei, M. Huang, Y. Yin, C. Jiang, S. Yang, G. Xing, S. Chen, C. Zhu, X. Hao, M. A. Green, and T. Chen, Hydrothermal deposition of antimony selenosulfide thin films enables solar cells with 10% efficiency, Nat. Energy **5,** 587 (2020).

[16] Y. Xu, R. Li, S. Bai, Y. Li, Z. Jia, Y. Yang, E. Cui, F. Yao, D. Wang, C. Lei, and Q. Lin, Chalcogenide-based narrowband photodetectors for imaging and light communication, Adv. Funct. Mater. **33,** 2212523 (2022).

[17] N. Huo, A. Figueroba, Y. Yang, S. Christodoulou, A. Stavrinidis, C. Magen, and G. Konstantatos, Engineering vacancies in Bi_2S_3 yielding sub-bandgap photoresponse and highly sensitive short-wave infrared photodetectors, Adv. Opt. Mater. **7,** 1900258 (2019).

[18] T. Wu, X. Zhou, H. Zhang, and X. Zhong, Bi_2S_3 nanostructures: A new photocatalyst, Nano Res. **3,** 379 (2010).

[19] G. Zhao, Y. Zheng, Z. He, Z. Lu, L. Wang, C. Li, F. Jiao, and C. Deng, Synthesis of Bi_2S_3 microsphere and its efficient photocatalytic activity under visible-light irradiation, Trans. Nonferrous Met. Soc. **28,** 2002 (2018).

[20] H. Song, X. Zhan, D. Li, Y. Zhou, B. Yang, K. Zeng, J. Zhong, X. Miao, and J. Tang, Rapid thermal evaporation of Bi_2S_3 layer for thin film photovoltaics, Sol. Energy Mater. Sol. Cells **146,** 1 (2016).

[21] C. Gao, H. Shen, L. Sun, and Z. Shen, Chemical bath deposition of Bi_2S_3 films by a novel deposition system, Appl. Surf. Sci. **257,** 7529 (2011).

[22] J. Lu, Z. Wang, Y. Zhang, and X. Zhou, Hydrothermal synthesis of Bi_2S_3 nanorods from a single-source precursor and their promotional effect on the photocatalysis of TiO_2, J. Nanomater. **2013,** 125409 (2013).

[23] J. Lu, Q. Han, X. Yang, L. Lu, and X. Wang, Preparation of Bi_2S_3 nanorods via a hydrothermal approach, Mater. Lett. **61,** 3425 (2007).

[24] D. Wang, C. Hao, W. Zheng, X. Ma, D. Chu, Q. Peng, and Y. Li, Bi_2S_3 nanotubes: Facile synthesis and growth mechanism, Nano Res. **2,** 130 (2010).

[25] J. Li, L. Jin, L. Fang, M. Zhang, Y. Wang, X. Jiang, J. Lv, G. He, and Z. Sun, Synthesis and characterization of Bi_2S_3 quantum dot-sensitized TiO_2 nanorod arrays coated with ZnSe passivation layers, Appl. Surf. Sci. **456,** 694 (2018).

[26] O. Karsandlk, Influence of thickness and annealing temperature on properties of solution processed bismuth sulfide thin films, J. Mater. Sci. **33**, 18014 (2022).

[27] W. Ji, X.-L. Shi, W.-D. Liu, H. Yuan, K. Zheng, B. Wan, W. Shen, Z. Zhang, C. Fang, Q. Wang, L. Chen, Y. Zhang, X. Jia, and Z. Chen, Boosting the thermoelectric performance of n-type Bi_2S_3 by hierarchical structure manipulation and carrier density optimization, Nano Energy **87**, 106171 (2021).

[28] M. Chen, H. Lu, N. M. Abdelazim, Y. Zhu, Z. Wang, W. Ren, S. V. Kershaw, A. L. Rogach, and N. Zhao, Mercury telluride quantum dot based phototransistor enabling high-sensitivity room-temperature photodetection at 2000 nm, ACS Nano **11**, 5614 (2017).

[29] L. Jiang, H. Huang, F. Gui, Y. Xu, and Q. Lin, Ultra-sensitive UV-NIR broadband phototransistors based on $AgBiS_2$-organic hybrid films, J. Mater. Chem. C **9**, 7583 (2021).

[30] Y. Kim, E. Jeong, M. Joe, and C. Lee, Synthesis of 2D semiconducting single crystalline Bi_2S_3 for high performance electronics, Phys. Chem. Chem. Phys. **23**, 26806 (2021).

[31] C. Kilcoyne, A. H. Ali, A. M. Alsaqqa, A. A. Rahman, L. Whittaker-Brooks, and G. Sambandamurthy, Gate-tunable transport characteristics of Bi_2S_3 nanowire transistors, Solid State Commun. **270**, 135 (2018).

[32] H. Zhu, C. A. Richter, E. Zhao, J. E. Bonevich, W. A. Kimes, H.-J. Jang, H. Yuan, H. Li, A. Arab, O. Kirillov, J. E. Maslar, D. E. Ioannou, and Q. Li, Topological insulator Bi_2Se_3 nanowire high performance field-effect transistors, Sci. Rep. **3**, 1757 (2013).

[33] Z. Liu, S. Peng, Q. Xie, Z. Hu, Y. Yang, S. Zhang, and Y. Qian, Large-scale synthesis of ultralong Bi_2S_3 nanoribbons via a solvothermal process, Adv. Mater. **15**, 936 (2003).

[34] Yanyan Li, Z. J., Yujie Yang, Fang Yao, Yong Liu, and Qianqian Lin, Shallow traps induced ultra-long lifetime of metal halide perovskites probed with light-biased time-resolved microwave conductivity, Appl. Phys. Rev. **10**, 011406 (2023).

[35] S. Wang, Y. Zhao, B. Che, C. Li, X. Chen, R. Tang, J. Gong, X. Wang, G. Chen, T. Chen, J. Li, and X. Xiao, A novel multi-sulfur source collaborative chemical bath deposition technology enables 8%-efficiency Sb_2S_3 planar solar cells, Adv. Mater. **34**, e2206242 (2022).

[36] See Supplemental Material at http://link.aps.org/supplemental/10.1103/PhysRevApplied.19.064080 for Supplementary Notes 1–3, Figures S1–S14, and Supplementary Video 1.

[37] S. Chattopadhyay, R. S. Kokenyesi, M. J. Hong, C. L. Watts, and J. G. Labram, Resolving in-plane and out-of-plane mobility using time resolved microwave conductivity, J. Mater. Chem. C **8**, 10761 (2020).

[38] O. G. Reid, D. T. Moore, Z. Li, D. Zhao, Y. Yan, K. Zhu, and G. Rumbles, Quantitative analysis of time-resolved microwave conductivity data, J. Phys. D **50**, 493002 (2017).

[39] C. S. Ponseca, M. Abdellah, K. Zheng, A. Yartsev, T. Pascher, T. Harlang, P. Chabera, T. Pullerits, A. Stepanov, J. P. Wolf, and V. Sundstrom, Organometal halide perovskite solar cell materials rationalized: Ultrafast charge generation, high and microsecond-long balanced mobilities, and slow recombination, J. Am. Chem. Soc. **136**, 5189 (2014).

[40] T. Han, M. Shou, L. Liu, Z. Xie, L. Ying, C. Jiang, H. Wang, M. Yao, H. Deng, G. Jin, J. Chen, and Y. Ma, Ultrahigh photosensitive organic phototransistors by photoelectric dual control, J. Mater. Chem. C **7**, 4725 (2019).

[41] F. Yao and Q. Lin, Charge carrier dynamics of organic cation-treated perovskites probed with time-resolved microwave conductivity, ACS Photonics **9**, 3165 (2022).

[42] A. Saeki, Y. Yasutani, H. Oga, and S. Seki, Frequency-modulated gigahertz complex conductivity of TiO_2 nanoparticles: Interplay of free and shallowly trapped electrons, J. Phys. Chem. C **118**, 22561 (2014).

[43] P. Prins, F. C. Grozema, J. M. Schins, S. Patil, U. Scherf, and L. D. Siebbeles, High Intrachain Hole Mobility on Molecular Wires of Ladder-Type Poly(p-phenylenes), Phys. Rev. Lett. **96**, 146601 (2006).

[44] M. Liu, H. Wang, Q. Tang, X. Zhao, Y. Tong, and Y. Liu, Ultrathin air-stable *n*-type organic phototransistor array for conformal optoelectronics, Sci. Rep. **8**, 16612 (2018).

[45] L. R. V. Buizza, A. D. Wright, G. Longo, H. C. Sansom, C. Q. Xia, M. J. Rosseinsky, M. B. Johnston, H. J. Snaith, and L. M. Herz, Charge-carrier mobility and localization in semiconducting Cu_2AgBiI_6 for photovoltaic applications, ACS Energy Lett. **6**, 1729 (2021).

[46] S. Kasap, *Photoconductivity and Photoconductive Materials: Fundamentals, Techniques and Applications* (Wiley-VCH, 2022).

[47] D. Han, M. H. Du, C. M. Dai, D. Sun, and S. Chen, Influence of defects and dopants on the photovoltaic performance of Bi_2S_3: First-principles insights, J. Mater. Chem. A **5**, 6200 (2017).

[48] D. Emin, C. H. Seager, and R. K. Quinn, Small-Polaron Hopping Motion in Some Chalcogenide Glasses, Phys. Rev. Lett. **28**, 813 (1972).

[49] H. Qiu, T. Xu, Z. Wang, W. Ren, H. Nan, Z. Ni, Q. Chen, S. Yuan, F. Miao, F. Song, G. Long, Y. Shi, L. Sun, J. Wang, and X. Wang, Hopping transport through defect-induced localized states in molybdenum disulphide, Nat. Commun. **4**, 2642 (2013).

[50] W. Lian, C. Jiang, Y. Yin, R. Tang, G. Li, L. Zhang, B. Che, and T. Chen, Revealing composition and structure dependent deep-level defect in antimony trisulfide photovoltaics, Nat. Commun. **12**, 3260 (2021).

[51] Y. Xu and Q. Lin, Photodetectors based on solution-processable semiconductors: Recent advances and perspectives, Appl. Phys. Rev. **7**, 011315 (2020).

[52] Y. J. Tak, D. J. Kim, W. G. Kim, J. H. Lee, S. J. Kim, J. H. Kim, and H. J. Kim, Boosting visible light absorption of metal-oxide-based phototransistors via heterogeneous In-Ga-Zn-O and $CH_3NH_3PbI_3$ films, ACS Appl. Mater. Interfaces **10**, 12854 (2018).

[53] G. Chen, Y. Yu, K. Zheng, T. Ding, W. Wang, Y. Jiang, and Q. Yang, Fabrication of ultrathin Bi_2S_3 nanosheets for high-performance, flexible, visible-NIR photodetectors, Small **11**, 2848 (2015).

[54] Y. Liu, P. Chen, G. Dai, W. Su, Y. Sun, J. Hou, N. Zhang, G. Zhao, Y. Fang, and N. Dai, Single $Bi_2S_3/Bi_2S_{3-x}O_x$ nanowire photodetector with broadband response from ultraviolet to near-infrared range, Phys. E Low Dimens. Syst. Nanostruct. **120**, 114041 (2020).

[55] F. X. Liang, C. W. Ge, T. F. Zhang, W. J. Xie, D. Y. Zhang, and L. B. Luo, Plasmonic hollow gold nanoparticles induced high-performance Bi_2S_3 nanoribbon photodetector, Nanophotonics **6**, 494 (2017).

[56] Gerasimos Konstantatos, L. Levina, Jiang Tang, and Edward H. Sargent, Sensitive solution-processed Bi_2S_3 nanocrystalline photodetectors, Nano Lett. **8**, 4002 (2008).